Frontiers in Heat and Mass Transfer

Tech Science Press

https://doi.org/10.32604/fhmt.2026.083008

ARTICLE

Energy and Exergy Evaluation Using Corrugated Multi-Ducts and Twisted Tape Inserts Applied to a Solar Air Heater: Experimental Research

Hussam J. Rashid, Mohammed K. Al-Saadi and Ameer Abed Jaddoa*

Electromechanical Engineering Department, University of Technology, Baghdad, Iraq

*Corresponding Author: Ameer Abed Jaddoa. Email: ameer.a.jaddoa@uotechnology.edu.iq

Received: 27 March 2026; Accepted: 08 May 2026; Published: 29 June 2026

ABSTRACT: An extensive experimental investigation was performed on the thermal, exergetic, and thermo-hydraulic performance of a corrugated multi-duct solar air heater (SAH) incorporating constrained twisted tape inserts under real outdoor conditions. A photovoltaic (PV)-powered DC blower was employed to supply the airflow, and four setups were tested: a smooth absorber plate, corrugated ducts, and corrugated ducts with one or two twisted tape inserts. The Reynolds number ranged from 2000 to 10,000. The results indicate that the configuration with two twisted tape inserts achieved the highest value of thermal efficiency under optimal operating conditions, with the useful heat gain increasing from about 100 W for the smooth case to 456 W. The Nusselt number increased by approximately 82% at low Reynolds numbers and 74% at high Reynolds numbers compared to the smooth configuration. Despite the related increase in the flow resistance, the thermo-hydraulic performance has improved significantly, with the thermo-hydraulic performance factor (THPF) reaching a highest value of about 1.9. Exergy analysis under optimal conditions revealed a maximum exergy efficiency of about 10.5% and a reduction in exergy destruction of approximately 9.7% compared to the smooth configuration. Furthermore, based on the experimental findings, empirical correlations for the Nusselt number and friction factor (FF) have been developed, and they show a strong agreement with the measured results, where the coefficient of determination (R^2) values reach 0.97 and the mean absolute percentage error (MAPE) values are below 5%, which validates the reliability of the proposed model for real SAH applications.

KEYWORDS: Solar air heater; corrugated multi-ducts; twisted tape inserts; exergy analysis

1 Introduction

Solar air heaters are commonly used in heating and drying applications because of their simple design and low cost, [1,2]. Solar energy, which is the most abundant renewable source of energy available, is widely used in these systems to supply clean and sustainable thermal energy used for building heating and for industrial processes [3–5]. The main drawbacks of traditional SAHs are the low convective heat transfer between absorber plate and the airflow. This constraint is due to the development of a viscous sub-layer adjacent to the surface of the absorber, which limits effective heat transfer [6–10]. Consequently, smooth duct configurations impose low thermal efficiency (ηth), due to reduced heat transfer between the absorber surface and the air flow [11–14].

Various surface modification techniques have been investigated to improve the thermo-hydraulic performance of SAHs by increasing turbulence and enhancing airflow mixing, thereby improving heat transfer. Mondloe et al. [15] conducted an experimental investigation on an SAH with transverse wire rib roughness under real outdoor conditions. The results demonstrated that thermal efficiency has enhanced

with a rise in airflow rate, reaching a maximum value of about 83.5%, while the exergy efficiency reached approximately 3.67%. Mahmood [16] have experimentally investigated glazed and unglazed SAHs with perforated absorber plates, where the glazed configuration showed higher outlet temperatures and thermal efficiency. Hussein et al. [17] examined the impact of pulsing airflow on a double-pass SAH and noted that outlet air temperature increased by 25.6%–27% and that the thermal efficiency was enhanced up to 15.2% compared with the steady flow. A double-pass SAH with V-shaped perforated fins was studied by Machi et al. [18], The thermal efficiency was enhanced by increasing heat transfer efficiency and achieving uniform flow over the absorber surface. A similar computational study on a jet impingement SAH was conducted by Pazarlıoğlu et al. [19], which reported An enhancement in the Nusselt number and thermal efficiency with increasing inlet Reynolds number and a decrease in pressure drop. Nidhul et al. [20] conducted an experimental and numerical investigation of the thermo-hydraulic and exergetic performance of a baffle-integrated flat-plate SAH for various configurations.

The proposed configuration achieved the highest thermo-hydraulic performance of 2.69, which indicated the improved ηth of 55%–70% and exergetic performance of 1.5%–2.2%, compared to 30%–55% and 0.9%–1.7% for a ribbed rectangular SAH. Abd et al. [21] introduced an experimental assessment of the energy and exergy performance of a double-pass SAH adopting a V-corrugated wire mesh absorber compared to a conventional V-corrugated plate. The outcomes indicated that the wire mesh method had the highest thermal and exergy performance of 87.3% and 4.4%, respectively, compared to the normal absorber, which had 65.1% and 3.4%, respectively. Alnakeeb et al. [22] performed a numerical analysis of a corrugated plate SAH featuring vortex generators within a Reynolds number range of 7000 to 25,000. The thermo-hydraulic and thermal performance was significantly improved with the utilization of the vortex generators, achieving a peak thermo-hydraulic performance value of 0.91 for rectangular vortex generators at Re = 7000 with an angle of attack of 30°. Abedalh and Mohammed [5] performed a numerical analysis of the thermal efficiency of an SAH utilizing corrugated absorber panels with varying V-groove angles. Results revealed that the thermal efficiency was 20.8%, 26.3%, and 36.14% higher than the flat plate for trough angles of 45°, 30°, and 15°, respectively, for solar irradiance of 900 W/m^2. Ghosh et al. [23] Conducted an experimental investigation of the thermal and exergy performance of a SAH utilizing hybrid tape vortex generators throughout a Reynolds number range between 10,794 to 73,644. The hybrid inserts increased the Nusselt number by 89% and the friction factor by only 35%, indicating improved heat transfer performance with a moderate increase in pressure drop. Bhattacharyya et al. [24] experimentally investigated mixed convection in an SAH tube equipped with twisted tape inserts to enhance heat transfer in the range of Reynolds numbers 563–10,240. The most effective improvement of heat transfer was observed at a twist ratio of 3, and correlations for Nusselt number and friction factor has established, exhibiting a peak divergence from the experimental data of approximately ±0.75%. Karthickmunisamy et al. [25] carried out an experimental assessment on an evacuated tube SAH adopting baffles and perforated twisted tape inserts at varying airflow velocities. The suggested scheme achieved the highest output temperature of 318.47 K at 100 kg/h, the highest ηth of 59.7% at 500 kg/h, and the highest exergy performance of 2.37% at 100 kg/h. The exergy efficiency decreased as the airflow velocity increased. Farhan et al. [26] performed analytical and numerical analyses of a v-corrugated SAH using twisted tape inserts across a wide range of Reynolds values. Maximum thermal and thermo-hydraulic efficiencies (17.5% and 17%, respectively, with N = 5) and a maximum useful heat gain of 29,290 W (an overall enhancement of 17% compared to the configuration without inserts) were obtained with the proposed configuration. Ayadi et al. [27] conducted a CFD simulation that considers 3D aspects of flow through the 3D numerical analysis of solar air heaters using corrugated absorber plates and perforated baffles.

Furthermore, a 27% improvement was achieved by the proposed design in thermal performance at Re = 5000. In contrast, pitch minimization resulted in a 10%–22% gain with the baffle pitch reduced to 80 mm

while the pressure drop increased. Chompookham et al. [28] conducted a numerical investigation of an SAH employing twisted multiple V-baffles under turbulent flow conditions. The optimal configuration yielded a peak thermal enhancement factor of 2.81 at Re = 3000; meanwhile, this design resulted in a 50% average reduction in the FF in comparison with classical multiple V-baffles, with similar effective heat transfer. Boussouar et al. [29] conducted a numerical investigation on the thermal performance of flat-plate SAH collectors using perforated transverse baffles with varying hole dimensions. At the Reynolds number of 8500, the optimal setup had a maximum Nusselt number of about 79.56, accompanied by 459 Pa in the pressure drop. Perforated baffles improved the heat transfer by increasing flow disruption and thus increasing air mixing inside the duct. Vortex generators demonstrated a significant enhancement in both heat transfer and thermo-hydraulic efficiency of the designs, with the highest value of performance of 0.91 obtained at Re = 7000 (angle of attack of 30°).

Multi-duct configurations provide a larger heat transfer area and more uniform airflow distribution compared to single-duct systems, which contributes to improving overall thermal performance.

However, most enhancement techniques rely on complex geometrical modifications that increase turbulence, which leads to higher pressure losses and increased irreversibility, thereby limiting overall system performance. Moreover, only limited experimental studies have investigated simplified corrugated multi-duct SAHs incorporating a limited number of twisted tape inserts under real outdoor operating conditions, particularly when powered by photovoltaic-driven DC systems.

Despite the extensive research on solar air heater enhancement techniques, limited studies have investigated the combined effect of corrugated multi-duct configurations with a limited number of twisted tape inserts under real outdoor conditions using a fully DC-powered system. In addition, most previous studies focused either on corrugated surfaces or twisted tape inserts individually, with limited attention to their combined thermo-hydraulic and exergetic performance. Therefore, the present study provides a comprehensive experimental evaluation of this combined configuration, which distinguishes it from previous investigations.

Therefore, the present study experimentally investigates the thermal, hydraulic, and exergetic performance of a corrugated multi-duct SAH incorporating a limited number of twisted tape inserts. The system is tested under real outdoor conditions using a fully DC-powered airflow system. Four configurations are examined to identify an optimal configuration that enhances heat transfer while maintaining acceptable pressure losses and reduced irreversibility as follows:

- smooth absorber plate (case 1).
- corrugated ducts (case 2).
- corrugated ducts with one twisted tape insert (case 3).
- corrugated ducts with two twisted tape inserts (case 4).

2 Experimental Setup

A corrugated multi-duct SAH was manufactured and assessed experimentally in Baghdad, Iraq. The scheme comprises a rectangular wooden-framed collector with overall dimensions of 1.0 m × 0.60 m × 0.11 m, presuming a productive absorber domain of 0.60 m^2. The entire scheme structure is pictured in Fig. 1. Galvanized steel sheets were used for the collector casing and internal air passages to validate physical integrity as well as reduced thermal inertia. However, the use of galvanized sheets will increase the overall weight of the system. The unit was installed facing south at a tilt angle of 35°, related to the geographical latitude of the testing site.

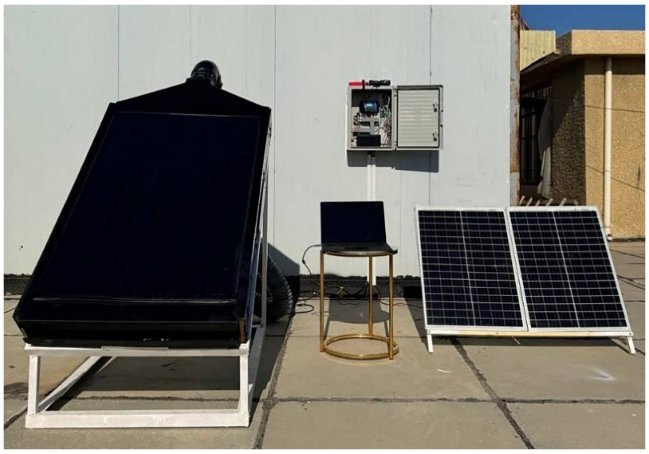

Figure 1: Schematic design and system formation of the SAH.

The SAH encompasses five comparable parallel corrugated air ducts to strengthen HT through surface-induced turbulence and upraised productive HT domain. The number of ducts was adopted to guarantee a uniform airflow issuance while holding realisable pressure losses and scheme elementariness within the collector operations.

Each duct has a length of 1.0 m, a width of 0.12 m, and a nominal height of 0.10 m. Corrugation is applied to both the upper and lower duct surfaces with a peak-to-trough depth of 0.02 m (e = 0.01 m), resulting in a minimum clear flow passage of approximately 0.08 m. The detailed geometry of the corrugated ducts is presented in Fig. 2. To intensify internal mixing, twisted tape inserts were employed as turbulence promoters, and four configurations were examined: smooth absorber plate, corrugated ducts without inserts, corrugated ducts with one twisted tape per duct, and corrugated ducts with two twisted tapes per duct.

Figure 2: Corrugated air ducts with twisted tapes configurations.

The airflow was generated using a 90 W DC blower. A standalone PV system equipped with two 50 W PV panels was used to power the device to ensure its entire operation under a DC power supply. A Pulse Width

Modulation (PWM) controller was used to regulate the airflow rate so that all experiments were conducted under similar operating conditions.

A pyranometer was used to measure the solar radiation intensity, and an anemometer was used to measure the velocity of air inside of the collector ducts, A digital manometer was employed to measure the pressure difference between the inlet and the output. Moreover, K-type thermocouples were used to measure the air inlet, air outlet, absorber, plate surface, and ambient temperatures. In addition, an Arduino-based data acquisition system was employed to record the experimental data, and before performing the measurements, all measuring instruments were calibrated based on standard procedure to ensure the accuracy of the measurements. Fig. 3 shows the PV-powered airflow system, points of pressure measurement, thermocouple, and the data acquisition unit.

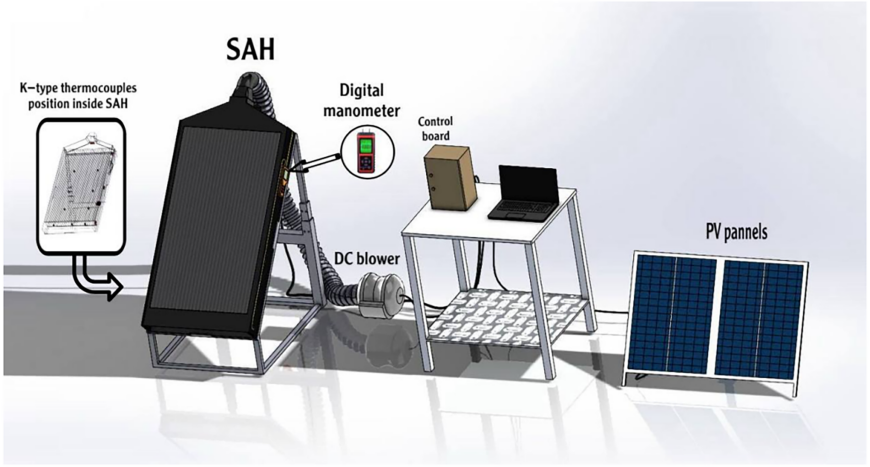

Figure 3: Picture of the proposed system under investigation.

All procedures of analysis were executed in cloudless weather during maximum solar exposure (09:00–16:00). Data were recorded hourly at invariable mass flow rates spanning from 0.02092 to 0.10459 kg/s after achieving an almost steady-state mode of operation to secure the uniformity and trustworthiness of the data obtained.

The roughness factors and flow optimization parameters considered in this study are listed in Table 1.

Table 1: Roughness factors and flow optimization parameters.

Parameter	Value
Relative corrugation pitch, p/e	2
Relative corrugation height (amplitude), e/H	0.10
Duct width to height ratio, W/H	1.2
Twist ratio, y/w	≈7
Number of twisted tapes per duct	0, 1, 2
Angle of tilt, β	35°

The geometric parameters of SAH are summarized in Table 2.

Table 2: Geometric parameters of the solar air heater.

Parameter	Value
Duct height, H	0.10 m
Duct width, W	0.12 m
Duct length, L	1.0 m
Number of air ducts	5
Absorber plate width	0.60 m
Absorber plate length	1.0 m
Absorber plate thickness	0.0008 m
Collector height	0.11 m
Glass cover thickness	0.005 m

The measurement uncertainties associated with the instruments used in the experimental setup are summarized in Table 3. All calculated parameters inherently include a degree of uncertainty. However, the estimated uncertainties are relatively small and do not significantly affect the observed trends or the validity of the obtained results.

Table 3: Instrument measurement uncertainty.

Measurement Device	Model/Brand	Unit	Range	Uncertainty
Pyranometer	TES-1333R	W/m^2	0–1999	±10 W/m^2
Anemometer	GM8901	m/s	0–30	±0.5%
K-type thermocouple	MAX6675 Module	°C	−40 to −1300	±0.25°C
Manometer	Testo 510	hpa	0–150	±0.1 hPa

3 Equations and Mathematical Expressions

The test results were gathered over two days in a row in Baghdad, Iraq, on January 3 and 4, 2026, when the weather was clear. Some of the things that were measured were the air temperature, the rate of mass flow, the drop in pressure, and the amount of sun energy. From 9:00 AM to 4:00 PM, every arrangement that was looked at was checked every hour.

The experiments were performed using several constant and distinct air mass flow rates in order to examine the thermal behavior of the SAH under different operating conditions. The selected mass flow rates were 0.02092, 0.04183, 0.06275, 0.08367, and 0.10459 kg/s, and the average values of the measured temperatures and solar radiation were used for the subsequent performance analysis. The selected mass flow rates were chosen to cover a representative range of Reynolds numbers under practical operating conditions of SAHs.

Based on the experimental data, a set of standard heat transfer and fluid flow relations was employed to evaluate the thermal and thermo-hydraulic performance of the SAH. These relations were used to determine the useful heat gain, convective heat transfer coefficient, Nusselt number, pressure drop, thermal efficiency, and thermo-hydraulic performance parameter. The governing equations applied in the present analysis are presented as follows.

In a rectangular duct, the air velocity V determine the mass flow rate of air across the SAH $\dot{m}$ as follows [30]:

$$\dot{m} = \rho \times V \times W \times H \tag{1}$$

The Reynolds number is calculated using the following relation [31]:

$$Re = \frac{\rho \times V \times D_h}{\mu} \tag{2}$$

where μ is the dynamic viscosity of air and D_h is the hydraulic diameter of the rectangular duct [32].

The hydraulic diameter is defined as:

$$D_h = \frac{2 \times W \times H}{W + H} \tag{3}$$

The rate of useful heat transfer is calculated as [33]:

$$Q_u = \dot{m} \times c_p \times (T_o - T_i) \tag{4}$$

where c_p is the specific heat capacity of air, T_i is the inlet air temperature, and T_o is the outlet air temperature.

The convective heat transfer coefficient between the absorber plate and the flowing air it is given by [34]:

$$h = \frac{Q_u}{A_p \times (T_p - T_f)} \tag{5}$$

where A_p is the absorber plate area and T_p is the average absorber plate temperature.

The average fluid temperature inside the duct is calculated as:

$$T_f = \frac{T_o + T_i}{2} \tag{6}$$

The Nusselt number is calculated using the following expression:

$$Nu = \frac{h \times D_h}{k} \tag{7}$$

where k is the thermal conductivity of air.

The FF is determined by the using the measured pressure drop as stated below:

$$f = \frac{2 \times \Delta P \times D_h}{\rho \times L \times V^2} \tag{8}$$

In the smooth case, the Blasius equation was employed to identify the reference FF f_s:

$$f_s = 0.79 \times Re^{-0.2} \tag{9}$$

The thermal efficiency of the SAH is calculated using the following relation:

$$\eta = \frac{Q_u}{A_p \times I} \times 100 \tag{10}$$

where I is the average solar radiation incident on the collector surface.

THPF is utilized to assess the combined effect of heat transfer enhancement and frictional losses. This parameter accounts for both the heat transfer enhancement and the associated increase in pressure drop due to disturbance of the flow. The THPF is defined as [35]:

$$THPF = \frac{(Nu_r/Nu_s)}{(f_r/f_s)^{1/3}} \tag{11}$$

where Nu_r and f_r are the Nusselt number and friction factor for the enhanced configuration, respectively, and Nu_s and f_s correspond to the smooth reference configuration.

4 Results and Discussion

The main objective of the present study is to assess the enhancement in thermal performance of the SAH under different operating configurations and to identify the case that provides optimal performance. The experiments were conducted under outdoor conditions during clear-sky days in January, during which the ambient temperature and solar radiation intensity were continuously monitored to ensure stable boundary conditions. The thermal, thermo-hydraulic, and hydraulic results presented in this section are subsequently interpreted using exergy analysis to provide a consistent assessment of irreversibilities and overall system performance. The average air temperature during the study was approximately 18°C whereas the mean instantaneous solar radiation received on the SAH surface was around 725 W/m^2, providing ideal conditions for measuring the thermal performance of the system. Thermal performance of SAHs are highly dependent on environmental conditions. In particular, the solar radiation intensity can be improved under moderate ambient temperature, which leads to a greater temperature gradient between the absorber surface and airflow, hence improving heat transfer performance. Fig. 4 illustrates the variation of solar radiation throughout the day and its effect on the average inlet air temperature. Fig. 5 presents the variation of the outlet air temperature for each investigated case under identical climatic conditions. The comparison provides a straightforward indication of SAH's thermal performance under equivalent conditions.

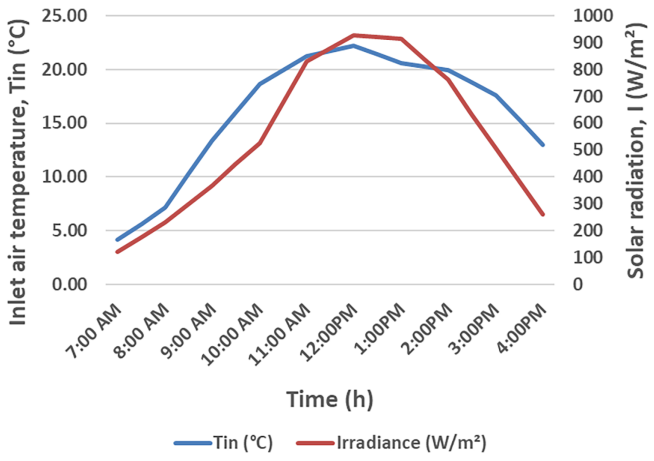

Figure 4: Average solar radiation and air inlet temperature during the period of experimental.

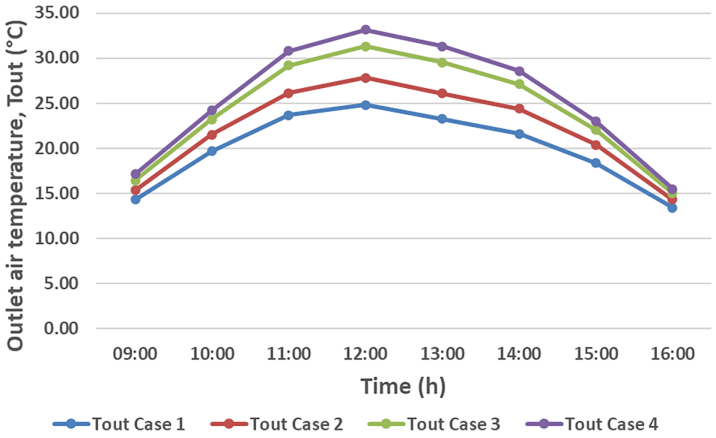

Figure 5: Average outlet air temperature with the time for different configurations.

Fig. 6 displays the behavior of the outlet air temperature for the four investigated cases under different conditions. The outlet temperature of air decreases as the flow rate rises owing to the reduced air residence time inside the collector. At low flow rates, Case 4 has an outlet temperature of approximately 44°C, compared to about 26°C for Case 1. This corresponds to an enhancement of about 69%. As the flow rate rises, the outlet temperature of air decreases; still, Case 4 maintains an improvement of approximately 17%–18% even at the highest flow rate. Case 3 exhibits the second-highest value of air outlet temperature, followed by Case 2, and Case 1 demonstrates the lowest values. It can be explained by the enhancement of turbulence and air mixing generated by the twisted tape, which improves the convective heat transfer between the plate of the absorber and the airflow.

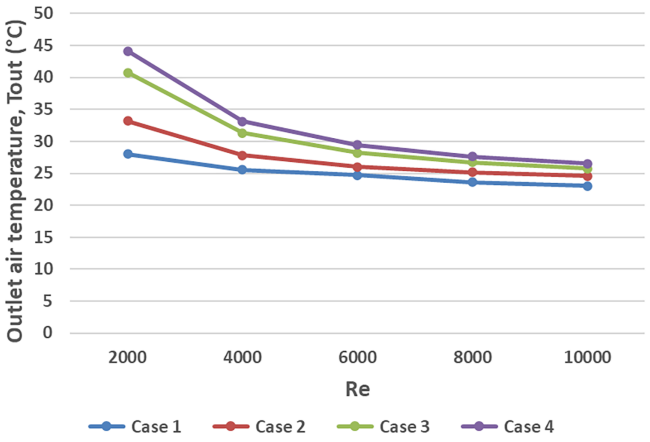

Figure 6: Average outlet air temperature for different configurations.

The Nusselt number and convective heat transfer rate increase with increasing flow rate, as shown in Figs. 7 and 8. This behavior is attributed to enhanced turbulence and improved air mixing inside the duct of SAH at higher air velocities, which increases in the convective heat transfer rate. Among all cases, Case 4 provides the highest enhancement.

The inverse relationship between FF and the Reynolds number for all cases were illustrated in Fig. 9. The FF decreased as the Reynolds number rose due to the inertial forces prevail over the viscous forces. Case 4 has the highest value of FF, followed by Case 3 and Case 2, and Case 1 keeps the lowest values.

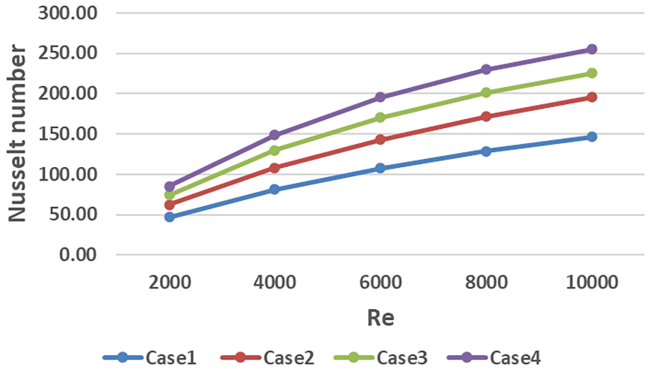

Figure 7: Average Nusselt number.

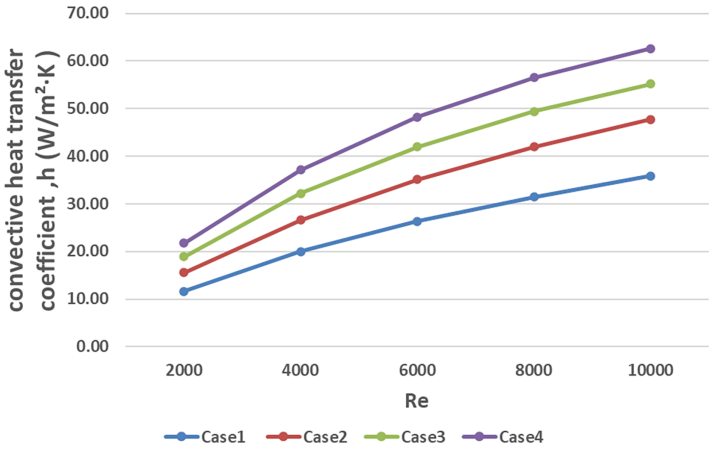

Figure 8: Convective heat transfer coefficient with Reynolds number.

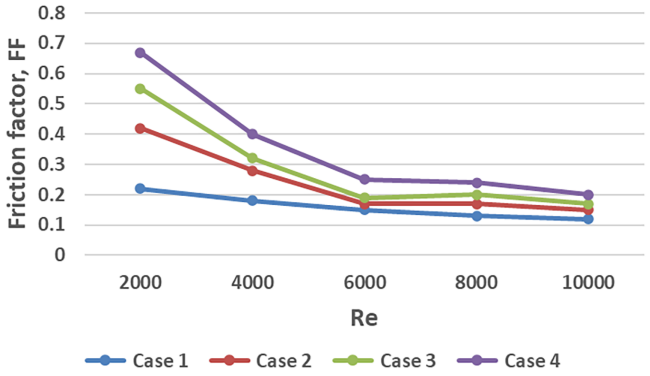

Figure 9: Friction factor with Reynolds number.

At Re = 10,000, FF of Case 4 is approximately 0.20 while corresponding values are 0.17 for Case 3, FF = 0.15 was for case 2 and 0.12 for case 1. These results indicate that flow modification enhances the resistance of flow. The decrease in FF at higher Reynolds numbers levels reflects a suitable balance between turbulence that has been increased and acceptable hydraulic losses.

The overall performance of the SAH is assessed by jointly using the THPF and thermal efficiency, which consider the heat transfer enhancement benefits as well as hydraulic penalties. As shown in Fig. 10, for all

the cases, THPF increases monotonically with the Reynolds number, confirming that thermal–hydraulic performance improves at high flow rates. Case 4 exhibited the highest THPF values that ranged from approximately 0.90 at Re = 2000 to around 1.90 at Re = 10,000, which serves to validate that the heat transfer improvement contributes more significantly than the increase in friction losses throughout all cases. Case 2 has the lowest THPF across the whole Reynolds number range, and Case 3 shows a moderate improvement.

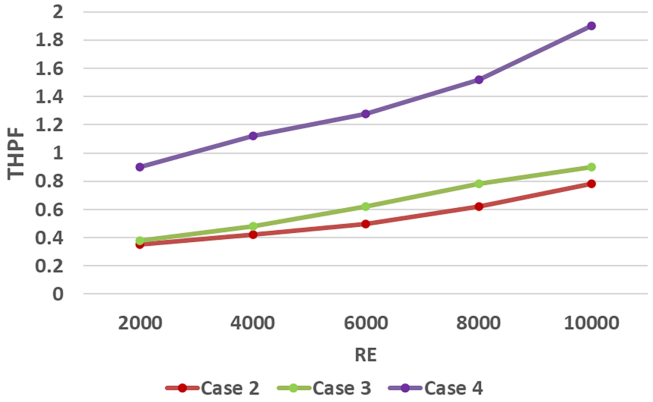

Figure 10: THPF with Reynolds number.

The behavior exhibited in Fig. 11 illustrates that there is a reasonably limited difference with the Re number. Additionally, case 4 maintains the maximum efficiency with a slight decrease as the Re number increases, while case 3 follows a similar but lower tendency. Case 2 and Case 1, on the other hand, show a gradual increase in the thermal efficiency because of the improvement in convective heat transfer. Increased turbulence and improved air mixing, promoted by twisted tape inserts, are the main reasons for the high thermal performance achieved in cases 3 and 4. These effects can reduce the thickness of the thermal boundary layer while enhancing the coefficient of convective heat transfer and thus could confirm improvement in heat transfer and overall thermal efficiency.

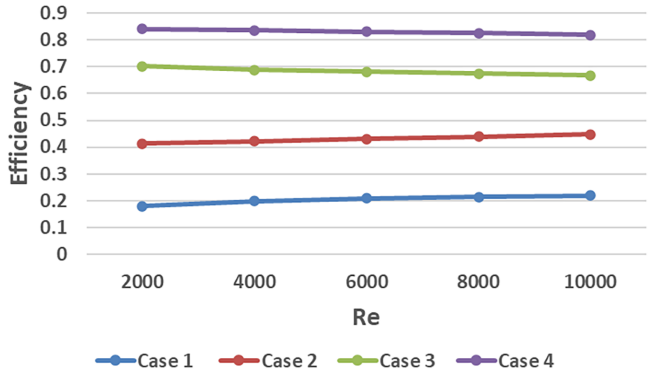

Figure 11: Thermal efficiency with the Reynolds numbers.

The modified cases demonstrate a direct relationship between the Reynolds number and the amount of pressure lost in the system as shown in Fig. 12. The higher the Reynolds number, the greater the pressure lost due to both increased flow velocity and increased friction from the surface roughness of the plate. In every modified case, the amount of pressure lost was greater than for Case 1 due to obstruction from multiple layers of plates and increased turbulence associated with many layers of plates. Case 4 exhibited the greatest

amount of pressure lost over all of the Reynolds number values, followed by Cases 3 and 2. Therefore, making changes in the geometry of the flow not only improves heat transfer but also increases hydraulic loss. This indicates that consideration needs to be given to a balance between improving heat transfer and reducing pressure losses.

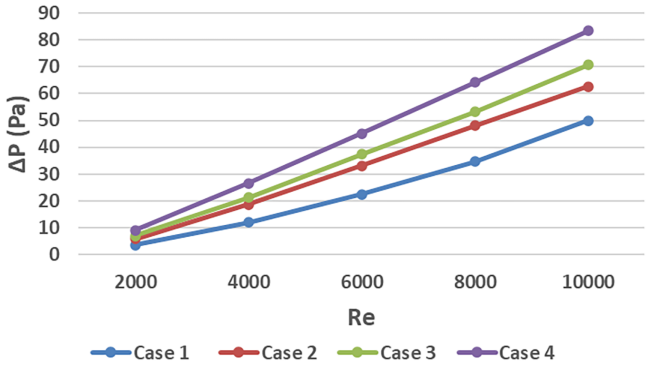

Figure 12: Pressure drop with the Reynolds numbers.

Fig. 13 as it varies throughout each day. In the morning there is a notable increase in output until this peak is reached at noon when all configurations experience their maximum gain of useful heat energy. After this peak occurs around noon, the output of all configurations then consistently declines through the afternoon until all configurations reach their minimum value at approximately 5:00 PM. The configuration with the largest amount of useful energy generated is Configuration 4 with 456 W at 12:00. In addition, although case 2 and case 3 did not provide as much heat energy when compared to the base case, both cases still provided more than case 1. Thus, changing the configuration of ducts can increase the mixing of the air that leads to increasing the convective heat coefficient that raises the energy efficiency in solar air heating systems.

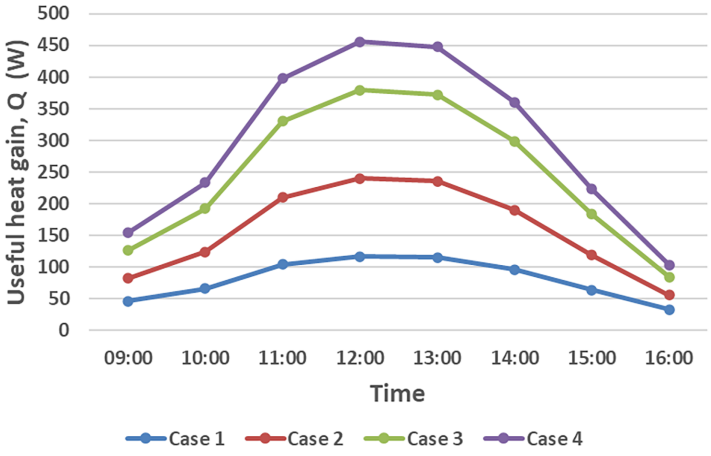

Figure 13: Useful heat gain with time.

The fan power-to-useful heat gain ratio decreases towards midday and increases again in the afternoon, as shown in Fig. 14. The highest values were observed for Case 1 and the lowest for Cases 3 and 4. Despite higher pressure losses for Case 4, it had more heat gain to compensate for the increased fan power, resulting in

a lower ratio than Case 3. This means that the additional configurations increased the thermal performance of SAH with no significant additional consumption of energy.

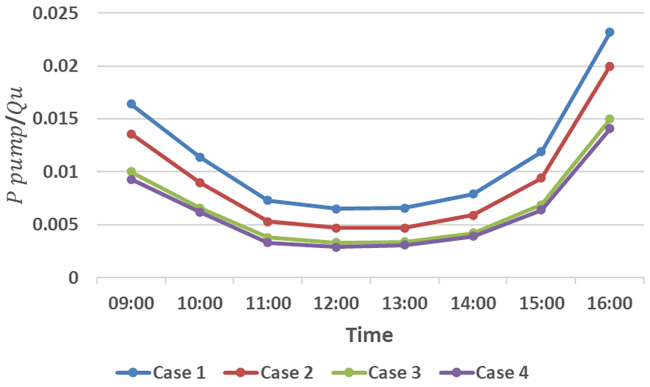

Figure 14: Ratio of pump power to useful heat gain.

5 Exergy Analysis

Exergy assessment is a strong thermodynamic measurement system used to measure how well energy is working and how much energy waste is attached to thermal systems. Where energy assessments are based on the preliminary law of thermodynamics, exergy assessments use the secondary law of thermodynamics to identify the total possible useful work as compared to the surroundings from a system. In addition, exergy assessment will also be used to assess the performance of proposed SAH designs for thermal fluid systems and to determine how the alteration of flow from the solar collector impacts the irreversibility and efficacy of the solar air heater. Methodological exergy assessment is based on formulations developed by Chand et al. [36].

5.1 Assumptions

For the purpose of the exergy analysis, the following assumptions are considered:

- The system operates under steady-state conditions during each measurement interval.
- Changes in kinetic and potential energy of air are neglected.
- Air behaves as a perfect gas with constant specific heat value.
- SAH, considered to be a control volume, had one inlet and outlet.
- Both of the heat transfer and work interactions are positive.

5.2 Exergy Balance Formulation

The general exergy balance equation for a control volume can be expressed as:

$$\sum \dot{E}x_{in} - \sum \dot{E}x_{out} = \dot{E}x_{dest} \tag{12}$$

where $\dot{E}x_{dest}$ represents the total exergy destruction within the system due to irreversibilities.

5.2.1 Exergy of Solar Radiation

The exergy associated with the incident solar radiation on the absorber surface is calculated using the Petela model as follows:

$$\dot{E}x_{solar} = IA_c \left[1 - \frac{4}{3}\left(\frac{T_{amb}}{T_{sun}}\right) + \frac{1}{3}\left(\frac{T_{amb}}{T_{sun}}\right)^4\right] \tag{13}$$

where I is the solar irradiance, A_c is the absorber area, T_{amb} is the ambient temperature, and T_{sun} is the effective sun temperature.

5.2.2 Flow Exergy of Air

The specific flow exergy of air at the inlet and outlet of the solar air heater is defined as:

$$\psi = (h - h_{amb}) - T_{amb}(s - s_{amb}) \tag{14}$$

Accordingly, the exergy rates at the inlet and outlet are given by:

$$\dot{E}x_{in} = \dot{m}\psi_{in} \tag{15}$$

$$\dot{E}x_{out} = \dot{m}\psi_{out} \tag{16}$$

5.2.3 Thermodynamic Properties of Air

The change in enthalpy of air between the outlet and inlet is expressed as:

$$h_{out} - h_{in} = C_p(T_{out} - T_{in}) \tag{17}$$

The change in entropy of air is given by:

$$s_{out} - s_{in} = C_p \ln\left(\frac{T_{out}}{T_{in}}\right) - R \ln\left(\frac{P_{out}}{P_{in}}\right) \tag{18}$$

where C_p is the specific heat of air and R is the gas constant.

5.2.4 Optical Exergy Loss

The optical exergy loss associated with the glass cover and absorber surface is calculated as:

$$\dot{E}x_{loss,optical} = (1 - \tau\alpha)IA_c\left[1 - \frac{4}{3}\left(\frac{T_{amb}}{T_{sun}}\right) + \frac{1}{3}\left(\frac{T_{amb}}{T_{sun}}\right)^4\right] \tag{19}$$

where τ and α represent the transmittance and absorptance of the glazing and absorber surface, respectively.

5.3 Exergy Destruction

By substituting the above relations into the exergy balance equation, the exergy destruction rate inside the solar air heater is obtained as:

$$\dot{E}x_{dest} = \dot{E}x_{solar} - \dot{m}C_p(T_{out} - T_{in}) + \dot{m}T_{amb}\left[C_p \ln\left(\frac{T_{out}}{T_{in}}\right) - R \ln\left(\frac{P_{out}}{P_{in}}\right)\right] - \dot{E}x_{loss,optical} \tag{20}$$

This expression is used to quantify the irreversibilities associated with heat transfer, pressure losses, and internal flow modifications within the solar air heater.

5.4 Exergy Efficiency

Exergy efficiency of SAH is defined as the ratio between useful exergy acquired by air stream and incident solar exergy input:

$$\eta_{ex} = \frac{\dot{E}x_u}{\dot{E}x_{solar}} \tag{21}$$

where the useful exergy rate transferred to the air stream is evaluated as the net increase in flow exergy between the outlet and inlet:

$$\dot{E}x_u = \dot{E}x_{out} - \dot{E}x_{in} = \dot{m}\left(\psi_{out} - \psi_{in}\right) \tag{22}$$

Accordingly, the final expression of the exergy efficiency can be written as:

$$\eta_{ex} = \frac{\dot{m}\left(\psi_{out} - \psi_{in}\right)}{\dot{E}x_{solar}} \tag{23}$$

This parameter is used for system exergetic performance comparison of various configurations under various operating conditions.

The exergy efficiency and the Reynolds number for all cases are shown in Fig. 15. It has been observed that with the increase of Reynolds number, the exergy efficiency decreases rapidly, meaning less utilization of useful exergy at high flow rates. Generally, the results show that Case 4 had the highest value of exergy efficiency, followed by Cases 3, 2, and 1. At Re = 2000, the maximum value of exergy efficiency was for Case 4, around 10.5%, decreasing to approximately 7.7% at Re ≈ 10,000, whereas Case 3 decreases from nearly 8.5% to approximately 6.4% within the same range of Reynolds numbers. In contrast, Case 1 keeps the lowest value of exergy efficiency, remaining below 3% for all ranges of Reynolds numbers. These results confirm that flow modification significantly enhances the exergetic performance of the system, although increasing the Reynolds number leads to diminishing returns in terms of exergy efficiency.

Fig. 16 summarizes the peak exergy efficiency of the four investigated configurations at different Reynolds numbers. It is clear that Case 4 often has the highest efficiency in the whole Reynolds number range, then Case 3, Case 2, and Case 1. The enhancement in the modified configurations confirms the positive effect of duct corrugation and twisted tape inserts on improving overall thermodynamic performance at peak operating conditions.

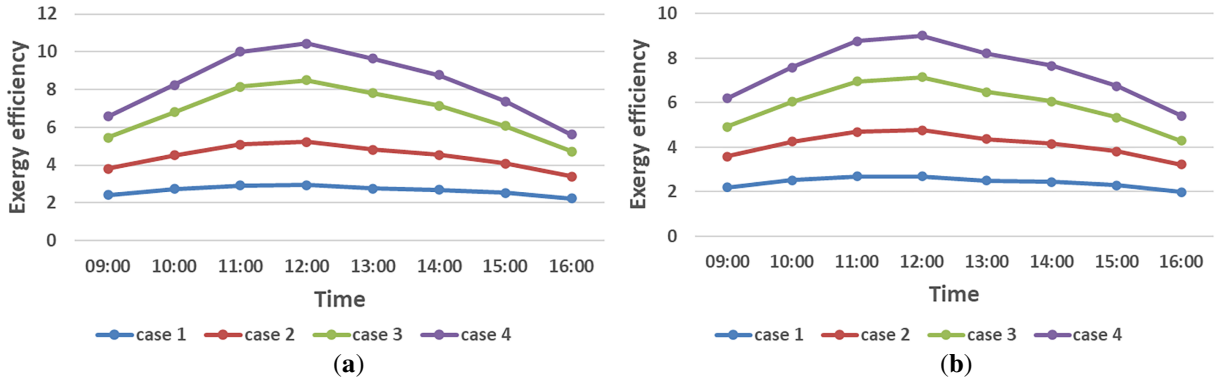

Figure 15: Continued

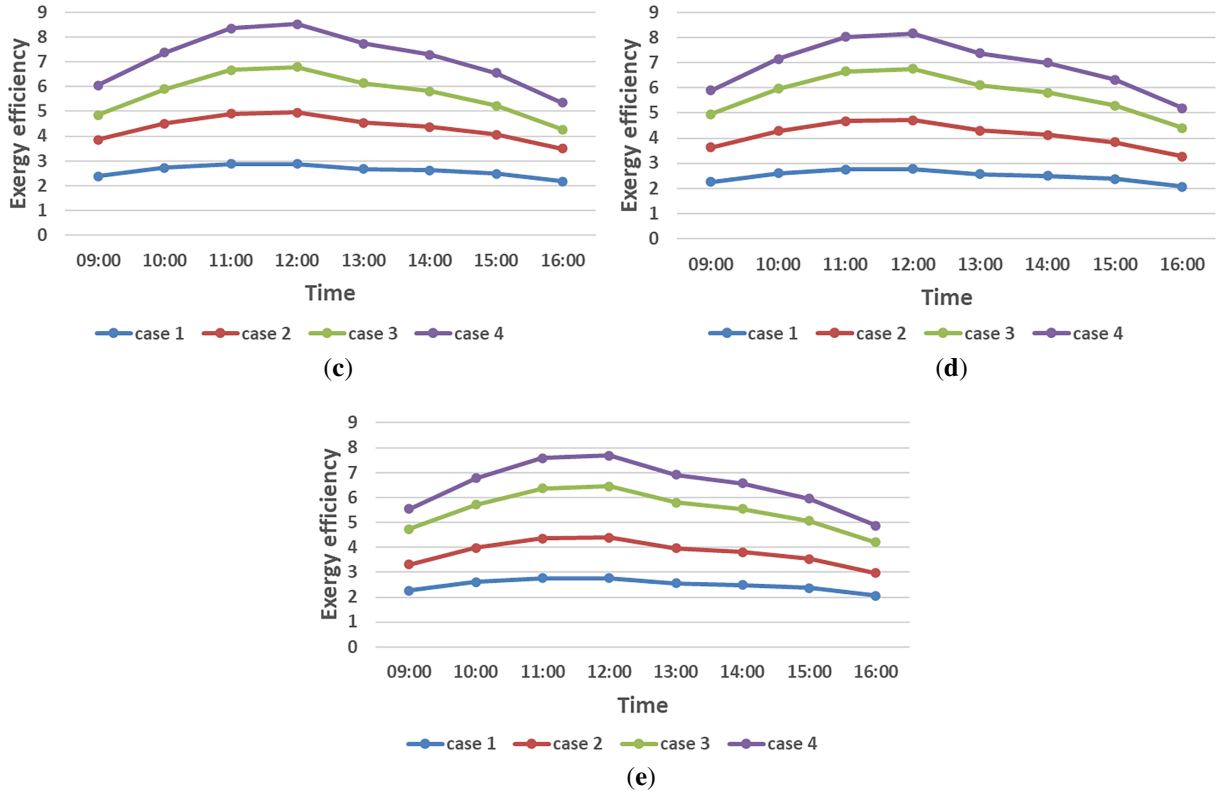

Figure 15: Peak-averaged exergy efficiency at different values of Reynolds numbers: (**a**) Re ≈ 2000; (**b**) Re ≈ 4000; (**c**) Re ≈ 6000; (**d**) Re ≈ 8000; (**e**) Re ≈ 10,000.

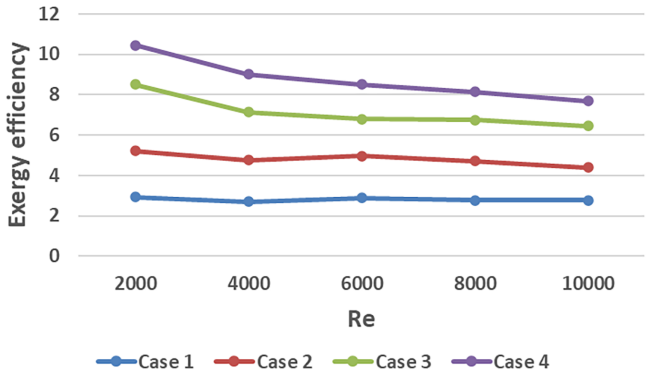

Figure 16: Exergy efficiency for different configurations.

Fig. 17 shows the exergy destruction fluctuation with the different range of Reynolds numbers for all investigated cases. Exergy destruction of all cases demonstrates a gradual growth with the Re number, indicating the existence of more irreversibility at high flow rates because of the enhancement of internal losses and thermodynamic dissipation.

Among the configurations, Case 1 exhibits the highest exergy destruction over the entire Reynolds number range, while Case 4 shows the lowest values, followed by Case 3 and Case 2. Case 1 exergy destruction is near 400 W at Re ≈ 2000, and drops to around 362 W for Case 4. As the Reynolds number increases to Re ≈ 10,000, the exergy destruction rises for all cases; however, Case 4 maintains the minimum irreversibility

level compared to the other configurations. The results show that not only does the flow modification increase exergy efficiency, but also the exergy destruction in the SAH is minimized, indicating that the flow modification is effective in increasing the exergetic performance of the system.

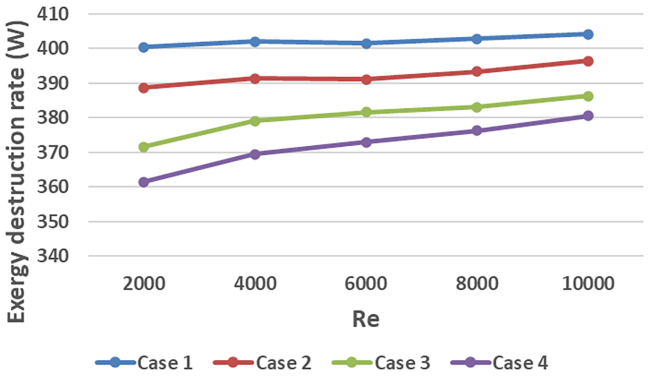

Figure 17: Exergy destruction rate with various Reynolds numbers.

6 Correlation

It is observed that both the Nusselt number and FF are strongly dependent on the Reynolds number and the geometrical characteristics of the flow obstructions. Accordingly, the functional relationships can be expressed as:

$$Nu = f_1(Re, Pr) \tag{24}$$

$$f = f_2(Re) \tag{25}$$

For forced convection, the Nusselt number is commonly correlated using a power-law relationship of the form:

$$Nu = A \times Re^n \tag{26}$$

where A represents the intercept and n represents the slope in the correlation line. The logarithmic form of Eq. (26) can be written as:

$$\log(Nu) = \log(A) + n \times \log(Re) \tag{27}$$

which can be solved by expressing it in a linear form as:

$$Y = C + m \times X \tag{28}$$

The Nusselt numbers obtained by experimentation were compared with the predicted values by the proposed correlations, as shown in Figs. 18 and 19. All configurations show a strong correlation between experimental and predicted values. This means that the reported coefficients of determination (R^2) shown in Table 4 were robust and approximated unity.

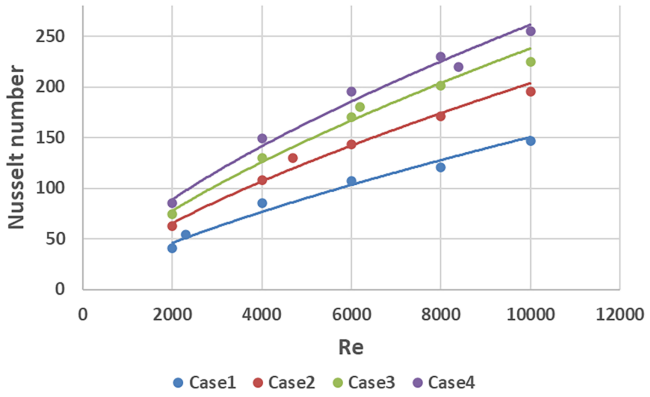

Figure 18: Correlation of Nusselt number.

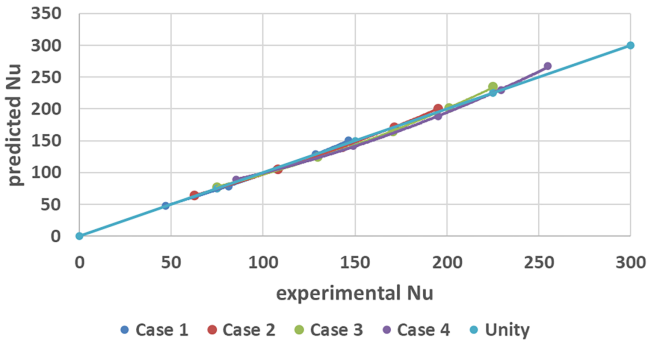

Figure 19: Predicted and experimental Nusselt numbers.

Table 4: A and n values of Nusselt number lines.

Case Number	A	n	R^2
1	0.218006	0.709927	0.995027
2	0.290674	0.709927	0.995027
3	0.408199	0.689856	0.989227
4	0.479451	0.686513	0.986054
Average	0.349082	0.699055	0.991333

The prediction accuracy was further evaluated using statistical error indicators. The RMSE values for Cases 1–4 were 2.481, 3.308, 5.540, and 7.131, respectively, while the corresponding AAD values were 2.066, 2.755, 4.589, and 5.929. The MAPE values also did not exceed 3.5%, in all cases, as well. These low error values confirm that the correlations proposed here allow a good prediction of the Nusselt number for the Reynolds number range investigated in this research.

The results obtained also match the general trends indicated in previous studies, i.e., with an increasing Reynolds number, the Nusselt number rises, and flow modification enhances heat transfer.

As a result of evaluating four experimental examples, the mean values for the interception point and the slope were found to be A = 0.3491 and n = 0.6991, respectively. The mean coefficient of determination calculated from these four examples was determined as R^2 = 0.9913, which provides evidence of a high

level of correlation between the relationship suggested and the experimentally obtained data. Therefore, the generalized Nusselt number relationship can be written as follows:

$$Nu = 0.3491 \times Re^{0.6991} \tag{29}$$

The Prandtl Number (Pr) is a parameter used in the correlation to represent the effect of fluid thermal properties on forced convection heat transfer. In many turbulent forced convection correlations, an exponent value of 0.4 is commonly used for Pr and is consistent with the correlations found in literature. It is important to mention that the Prandtl number was kept relatively constant for the operating conditions analyzed, and no experiments were conducted varying it. Thus, its inclusion in the correlation is based on the established role that it plays in forced convection correlations reported in the literature. The extended form of the correlation is given as:

$$Nu = 0.3491 \times Re^{0.6991} \times Pr^{0.4} \tag{30}$$

The influence of flow dynamics (Reynolds number) and thermal nature (Prandtl number) of working fluids will be considered in detail by this formulation. For the assessment of the accuracy of the mathematical modeling and error propagation, we compare the Nusselt number (Nusselt) values predicted by the model with experimental data for each case (1 through 4). The difference between each data point will be referred to as the prediction error for that value.

$$\varepsilon_c = Nu_{ref,i} - Nu_c \tag{31}$$

where i denotes the data point index and c represents the specific case.

The absolute error is calculated as:

$$Error = \mid \varepsilon_c \mid \tag{32}$$

and the relative error is obtained by dividing the absolute error by the corresponding experimental value as:

$$\frac{\varepsilon_c}{Nu_{ref,i}} \tag{33}$$

This mathematical model is applied for evaluating the Nusselt number prediction accuracy, and the same procedure is also adopted for the friction factor. All error calculations were performed using Excel as indicated in the previously stated error analysis results.

The Root Mean Squared Error (RMSE) for all cases was found by comparing the experimental and predicted values of the friction factor with those by the developed correlation. The RMSE values were found to be 0.00438, 0.01511, 0.01509, and 0.01835 for Case 1, 2, 3, and 4, as illustrated in Figs. 20 and 21.

The Mean Absolute Error (MAE) for the corresponding cases was 0.00376, 0.01282, 0.01319, and 0.01524, respectively. In addition, the Mean Absolute Percentage Error (MAPE) values were calculated as 2.203%, 5.120%, 4.579%, and 4.153%, respectively.

The statistical indicators from Table 5 shows that the determination coefficient R^2 is between the values of 0.978 and 0.985 with an average value of approximately equal to 0.972, indicating substantial agreement between experimental and predicted FF values. Thus, it is validated that the proposed FF correlation provides a very high degree of prediction accuracy and can be reliably used to estimate the FF for all cases investigated in this study, across the examined range of Reynolds numbers.

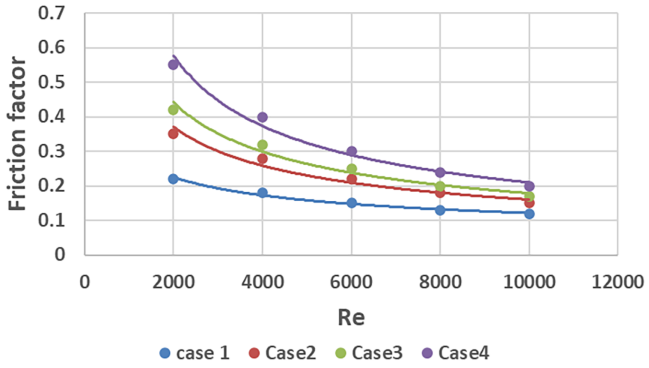

Figure 20: Correlation of friction factor.

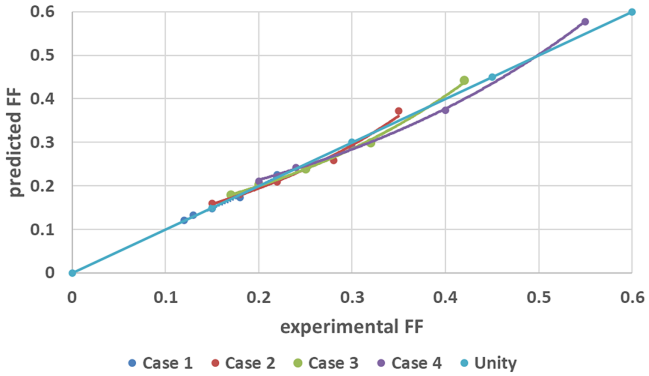

Figure 21: Predicted and experimental friction factor.

Table 5: Values of A and *n* of FF lines.

Case Number	B	m	R^2
1	4.206120	−0.384867	0.985479
2	19.723520	−0.522478	0.955597
3	31.858382	−0.562748	0.971734
4	68.986095	−0.629187	0.978661
Average	31.19353	−0.52482	0.972868

Most of the data points for all four cases stray only slightly from, or actually lie on, the unity line, showing that it is capable of predicting the general behavior of FF experimental data. Minor deviations observed in some regions suggest that, depending on the flow conditions—particularly at lower or higher Reynolds numbers—the correlation may slightly overpredict or underpredict the friction factor values. These deviations remain within acceptable limits and are quantitatively summarized in Table 5, confirming the reliability of the proposed correlation.

7 Limitations of the Study

This study has particular limitations. Using galvanized steel increases the overall weight of the system, potentially affecting its installation for building applications. Moreover, the experiments were performed under specific outdoor climatic conditions on days with clear-sky and different weather conditions may

affect the system performance. Despite these limitations, the obtained results provide a reliable basis for the performance evaluation of the proposed design of SAHs.

8 Conclusion

This experimental study assessed the thermal and thermo-hydraulic performance of a corrugated multi-duct solar air heater with twisted tape inserts under real outdoor conditions.

- Convective heat transfer coefficient and the Nusselt number: For all investigated configurations, the convective heat transfer coefficient and Nusselt number have been increased with the Reynolds number. The Nusselt number was highest at about 255 when Re ≈ 10,000 in case 4, where there were two twisted tape inserts. This result reflects the strong effect of flow disturbance and enhanced mixing in improving convective heat transfer.
- Friction factor: For all cases, the FF decreased as the Reynolds number increased. At Re ≈ 10,000, case 4 had a friction factor of approximately 0.20, while case 3 had 0.17, case 2 had 0.15, and case 1 had 0.12, reflecting the hydraulic penalty associated with the modification of flow.
- Thermal performance: With duct modification made, thermal output improved greatly (maximum useful heat gain = approximately 456 W at peak operating conditions). All enhanced configurations outperformed the smooth plate at peak performance (case 4). This enhancement is attributed primarily to the increased turbulence, which leads to improved heat transfer due to the mixing of the flow.
- Thermo-hydraulic performance factor: THPF for all configurations improved with Reynolds number; the best overall THPF was obtained from case 4 (THPF ≈ 1.90) when Re ≈ 10,000, indicating that enhancements to thermal performance outweighed any effects of pressure drops.
- Results of exergy analyses indicate large gains were realized for the utilization of energy quality with the use of flow alteration; exergy efficiency was maximized at approximately 10%–11% under the worst-performing condition, whereas a smooth absorbent plate performed below 3%. This is attributed to improved energy utilization and reduced irreversibility due to enhanced turbulence and flow mixing.
- All cases saw an increase in exergy destruction rate with Reynolds number; however, modified designs saw a lower level of irreversibility than smooth plates. At Re = 2000, Case 4 possessed the least value of exergy destruction (385 W) compared to Case 1, which had 400 W. That indicating the enhanced configurations reduce thermodynamic losses despite increased flow disturbances.
- The correlation between Nusselt number and friction factor showed good correlation (R^2 >= 0.95) between experimental and predicted data, lending credence to the use of both measured metrics for accurate prediction of heat transfer and hydraulic performance through the range of Re investigated.
- Taken together, these findings support the theory that incorporating both properties (i.e., multi-ducts with few twisted tape inserts) provides an effective means of enhancing heat transfer capability and thermal and hydraulic performance, as well as exergy efficiency for exposed (or practical) solar air heating applications.

Additional work could be completed from this project using CFD analysis techniques to examine localized heat transfer, flow morphed structures, and distribution of irreversibility through the interior of the ducts. More comprehensive experimental work examining alternate duct configurations and longer/new operational parameter ranges is warranted in order to fully validate these findings and produce a repeatable study.

Acknowledgement: We would like to express our genuine gratitude toward University of Technology that kindly have support this work.

Funding Statement: The authors received no specific funding for this study.

Author Contributions: Study conception and design: Hussam J. Rashid, Mohammed K. Al-Saadi and Ameer Abed Jaddoa; data collection: Hussam J. Rashid, Mohammed K. Al-Saadi and Ameer Abed Jaddoa; analysis and interpretation of results: Hussam J. Rashid, Mohammed K. Al-Saadi and Ameer Abed Jaddoa; draft manuscript preparation: Hussam J. Rashid, Mohammed K. Al-Saadi and Ameer Abed Jaddoa. All authors reviewed and approved the final version of the manuscript.

Availability of Data and Materials: The manuscript contains the complete data needed to support this work.

Ethics Approval: Not applicable.

Conflicts of Interest: The authors declare no conflicts of interest.

References

1. Dović D, Andrassy M. Numerically assisted analysis of flat and corrugated plate solar collectors thermal performances. Sol Energy. 2012;86(9):2416–31. doi:10.1016/j.solener.2012.05.016.
2. Ghafoor MSA, Al-Saadi MK, Jaddoa AA. Comparative study on the performance of a solar air heater using aluminum soda cans with different arrangements. Front Heat Mass Transf. 2025;23(3):975–90. doi:10.32604/fhmt.2025.064025.
3. Habeeb GA, Jaddoa AA, Alkhasraji JMD. A numerical study of the solar air heater performance using artificial spherical obstacles. Int J Heat Technol. 2025;43(2):703–20. doi:10.18280/ijht.430230.
4. Shafi STA, Al-Saadi MK, Jaddoa AA. Improving solar air heater performance using novel perforated V-shaped barriers: experimental study. Terra Joule J. 2025;1(1):4. doi:10.64071/3080-5724.1005.
5. Abedalh AS, Mohammed SH. Numerical investigation of thermal performance of solar air heater using different angle V-grooved corrugated absorber plate. Front Heat Mass Transf. 2023;21(1):227–43. doi:10.32604/fhmt.2023.041777.
6. Zubairi LT, Danismaz M, Yasin NJ, Al-Shohani WAM. Comparative analysis of thermal performance in dual-flow solar air heaters utilizing diverse absorber plates. Int J Heat Technol. 2023;41(4):1014–34. doi:10.18280/ijht.410423.
7. Hegde AK, Pai R, Karanth KV. Energy and exergy analysis of a cross-flow solar air heater for thermohydraulic performance augmentation. Int J Therm Sci. 2023;194:108577. doi:10.1016/j.ijthermalsci.2023.108577.
8. Goel V, Hans VS, Singh S, Kumar R, Pathak SK, Singla M, et al. A comprehensive study on the progressive development and applications of solar air heaters. Sol Energy. 2021;229(2):112–47. doi:10.1016/j.solener.2021.07.040.
9. Abushanab WS, Zayed ME, Sathyamurthy R, Moustafa EB, Elsheikh AH. Performance evaluation of a solar air heater with staggered/longitudinal finned absorber plate integrated with aluminium sponge porous medium. J Build Eng. 2023;73:106841. doi:10.1016/j.jobe.2023.106841.
10. Habeeb GAH, Jaddoa AA, Alkhasraji JMD. Effect of the absorber surface roughness on the performance of a solar air collector: an experimental analysis. Int J Heat Technol. 2025;43(4):1276–86. doi:10.18280/ijht.430407.
11. Chabane F, Moummi N, Benramache S, Bensahal D, Belahssen O. Collector efficiency by single pass of solar air heaters with and without fins. Eng J. 2013;17(3):43–55. doi:10.4186/ej.2013.17.3.43.
12. Nayak RK, Prasad RS, Nayak UK, Gupta AK. Performance analysis of longitudinal fin jet plate solar air heater under cross-flow condition. Front Heat Mass Transf. 2022;19:1–12. doi:10.5098/hmt.19.22.
13. Alam T, Kim MH. Performance improvement of double-pass solar air heater: a state-of-the-art review. Renew Sustain Energy Rev. 2017;79:779–93. doi:10.1016/j.rser.2017.05.087.
14. Sabet GS, Sari A, Fakhari A, Afsarimanesh N, Organ D, Hoseini SM. An experimental and numerical thermal flow analysis in a solar air collector with different delta wing height ratios. Front Heat Mass Transf. 2024;22(2):491–509. doi:10.32604/fhmt.2024.048290.
15. Mondloe DS, Ghritlahre HK, Agrawal GK. Evaluation of energetic and exergetic performance of solar air heater using transverse wire rib roughness with various gaps: experimental study. J Eng Appl Sci. 2025;72(1):89. doi:10.1186/s44147-025-00632-w.
16. Mahmood AJ. Experimental investigation of thermal efficiency, heat losses, and economic feasibility of glazed and unglazed solar air heaters. Results Eng. 2025;27(1):106004. doi:10.1016/j.rineng.2025.106004.

17. Hussein N, Ahmed S, Ekaid A. Thermal performance of a counter-flow double-pass solar air heater with steady and pulsating flow. Eng Technol J. 2022;41(1):176–84. doi:10.30684/etj.2022.135475.1274.
18. Machi MH, Farkas I, Buzas J. Enhancing thermal efficiency of double-pass solar air collectors: a comparative study on V-angled perforated fins. Energy Rep. 2024;12:481–94. doi:10.1016/j.egyr.2024.06.048.
19. Pazarlıoğlu HK, Tepe AÜ, Tekir M, Arslan K. Effect of elongated jet hole design on thermal efficiency of solar air heater. Therm Sci Eng Prog. 2022;36:101483. doi:10.1016/j.tsep.2022.101483.
20. Nidhul K, Yadav AK, Anish S, Arunachala UC. Thermo-hydraulic and exergetic performance of a cost-effective solar air heater: CFD and experimental study. Renew Energy. 2022;184(3):627–41. doi:10.1016/j.renene.2021.11.111.
21. Abd HM, Abdulrazzaq NM, Soheel AH. Solar air heater energy and exergy enhancement using a V-corrugated wire mesh absorber: experimental comparison. Energy. 2024;309(2):133136. doi:10.1016/j.energy.2024.133136.
22. Alnakeeb MA, Hassan MA, Teamah MA. Thermal performance analysis of corrugated plate solar air heater integrated with vortex generator. Alex Eng J. 2024;97:241–55. doi:10.1016/j.aej.2024.04.019.
23. Ghosh S, Bhattacharyya S, Halder B, Biswas N, Biswas S. Exergy and thermal performance analysis of solar air heater with hybrid tape vortex generators. Sol Energy. 2025;301(3):113954. doi:10.1016/j.solener.2025.113954.
24. Bhattacharyya S, Vishwakarma DK, Soni MK. Experimental investigation of twisted tape-induced mixed convection for optimized thermofluidic performance. Int Commun Heat Mass Transf. 2025;164(17):108865. doi:10.1016/j.icheatmasstransfer.2025.108865.
25. Karthickmunisamy T, Veerakumar A, Vijayan S, Venkatramanan R. Experimental investigation of an evacuated tube solar air heater with baffles and perforated twisted tapes. Proc Inst Mech Eng E. 2025;240(2):1267–80. doi:10.1177/09544089251368623.
26. Farhan AA, Ali MA, Ahmed HE. Energetic and exergetic efficiency analysis of a V-corrugated solar air heater integrated with twisted tape inserts. Renew Energy. 2021;169:1373–85. doi:10.1016/j.renene.2021.01.109.
27. Ayadi B, Hajlaoui K, Mohsen AM, Alizadeh A, Shaban M, Aich W, et al. Enhancing solar air heater performance using corrugated plates and perforated baffles. Sci Rep. 2025;15(1):45773. doi:10.1038/s41598-025-28600-7.
28. Chompookham T, Eiamsa-ard S, Buanak K, Promvonge P, Maruyama N, Hirota M, et al. Thermal performance augmentation in a solar air heater with twisted multiple V-baffles. Int J Therm Sci. 2024;205(3):109295. doi:10.1016/j.ijthermalsci.2024.109295.
29. Boussouar G, Rostane B, Aliane K, Ravi D, Gęca MJ, Gola A. Thermal performance of solar air collectors with and without perforated baffles. Energies. 2024;17(15):3812. doi:10.3390/en17153812.
30. Alam T, Saini RP, Saini JS. Experimental investigation of thermohydraulic performance of a rectangular solar air heater duct equipped with V-shaped perforated blocks. Adv Mech Eng. 2014;6:948313. doi:10.1155/2014/948313.
31. Alam T, Saini RP, Saini JS. Effect of circularity of perforation holes in V-shaped blockages on heat transfer and friction characteristics of rectangular solar air heater duct. Energy Convers Manag. 2014;86:952–63. doi:10.1016/j.enconman.2014.06.050.
32. Lertnuwat B. Effect of number and placement of punched holes in rectangular winglet vortex generators on solar air heater performance. Energy Convers Manag X. 2024;24:100714. doi:10.1016/j.ecmx.2024.100714.
33. Aouissi Z, Chabane F, Teguia MS, Bensahal D, Moummi N, Brima A. Determination of heat transfer coefficient by convection according to baffle shape in solar air collectors. J Renew Energy. 2022;25(1). doi:10.54966/jreen.v25i1.1070.
34. Kumar A, Layek A. Nusselt number and friction factor correlation of solar air heater having twisted-rib roughness on absorber plate. Renew Energy. 2019;130(1):687–99. doi:10.1016/j.renene.2018.06.076.
35. Bezbaruah PJ, Kumar R, Das RS. Thermohydraulic performance analysis of solar air heater with helical roughness. In: Proceedings of the 25th National and 3rd International ISHMT-ASTFE Heat and Mass Transfer Conference (IHMTC-2019); 2019 Dec 28–31; Roorkee, India. p. 233–7. doi:10.1615/IHMTC-2019.400.
36. Chand S, Ghritlahre HK, Singh AP. Exergetic performance evaluation of louvered finned solar air heater: experimental investigation. J Eng Appl Sci. 2024;71(1):145. doi:10.1186/s44147-024-00478-8.